AJG

Article

Adaptive Polarimetric Orientation Angle Correction and Scattering Decomposition for Robust Man-Made Structure Extraction in Polarimetric Synthetic Aperture Radar Data

Yasumin Siriprathan*[1], Junichi Susaki[2], and Yoshie Ishii[3]

Graduate School of Engineering, Kyoto University, Kyotodaigaku Katsura, Nishikyoku, Kyoto 615-8540, Japan

[1]<siriprathan.yasumin.64u@st.kyoto-u.ac.jp>, [2]<susaki.junichi.3r@kyoto-u.ac.jp>,

[3]<ishii.yoshie.4k@kyoto-u.ac.jp>

*Corresponding author: Y. Siriprathan, Email: <siriprathan.yasumin.64u@st.kyoto-u.ac.jp>

Received: December 17, 2025; Accepted: March 26, 2026; Published: April 5, 2026

ABSTRACT

Accurate extraction of man-made structures is essential for urban planning and disaster management, yet conventional Polarimetric Synthetic Aperture Radar (PolSAR) methods often suffer from orientation-induced scattering ambiguity and confusion between buildings and vegetation in complex urban environments. This study presents a physics-informed framework for detecting vertical structures using ALOS-2/PALSAR-2 data. The method integrates experimental backscattering knowledge with satellite-scale analysis through three refinements: (1) confidence-based Polarimetric Orientation Angle (POA) correction, (2) adaptive scattering decomposition to rebalance double-bounce and volume components, and (3) Region of Interest–based statistical refinement to improve class separability. Machine learning models trained on microwave backscattering measurements from concrete blocks were applied to satellite data using Random Forest classification. Validation across Tokyo, Bangkok, and Manila achieved over 94%, representing 15–20 percentage point improvements over baseline methods. The refined approach significantly reduces misclassification in mixed-scattering regions and demonstrates strong robustness and transferability across diverse urban environments.

Keywords: Man-made structure extraction, Polarimetric synthetic aperture radar, Scattering decomposition, Polarimetric orientation angle

1. INTRODUCTION

The rapid pace of urbanization, particularly in Asia, has created substantial challenges in infrastructure development, environmental sustainability, and disaster risk management (United Nations, 2019). Accurate identification and mapping of man-made structures such as buildings, factories, and other vertical constructions are essential for applications including urban planning, infrastructure monitoring, and post-disaster assessment (Weng, 2012). Traditional approaches based on optical imagery and Geographic Information Systems (GIS) can be affected by persistent cloud cover and atmospheric conditions, which limit data

availability in many regions. In addition, while revisit frequency and temporal resolution of modern optical sensors have significantly improved, their performance remains constrained under adverse weather and illumination conditions, reducing their reliability for continuous urban monitoring (Schmitt and Zhu, 2016).

Polarimetric Synthetic Aperture Radar (PolSAR) has emerged as a powerful tool for extracting urban areas due to its all-weather, day-and-night imaging capabilities and sensitivity to scattering mechanisms (Lee and Pottier, 2009). Numerous studies have leveraged model-based decomposition techniques, such as the Freeman-Durden three-component model (Freeman and Durden, 1998) and Yamaguchi's four-component extension (Yamaguchi et al., 2006), to characterize scattering contributions from natural and urban surfaces. However, these decompositions face difficulties in urban environments because of the overlapping scattering signatures between buildings, vegetation, and flat surfaces such as roads.

One critical factor influencing decomposition accuracy is the Polarimetric Orientation Angle (POA). Building orientation in densely built areas can induce POA shifts, causing misinterpretation of scattering mechanisms. Kimura (2008) reported that POA variations often lead to confusion between buildings and vegetation, while Li et al. (2016) highlighted the sensitivity of decomposition outputs to POA estimation errors. Although several studies have proposed POA incorporation for improved classification, its instability in heterogeneous urban areas remains a persistent limitation.

To address this issue, we propose a PolSAR-based classification method for extracting vertical man-made structures while explicitly excluding flat surfaces such as roads and runways. Our approach is guided by experimental backscattering observations showing that unstable or ambiguous POA values frequently correspond to misclassification at the boundaries between urban and natural areas (Kajimoto and Susaki, 2013; Lee et al., 2002).

The proposed method consists of three main components: (1) confidence-guided POA correction to stabilize orientation estimates and reduce the impact of unreliable pixels, (2) adaptive scattering decomposition based on a modified Yamaguchi model to emphasize the contrast between man-made and natural features (Yamaguchi, 2020; Cloude and Pottier, 1996), and (3) Region of Interest (ROI) based statistical refinement to apply localized statistics for adjusting thresholds and mitigating variability in scattering behavior.

The resulting feature sets are integrated into a Random Forest (RF) classifier (Breiman, 2001) to improve robustness in complex urban environments. The methodology was tested using Advanced Land Observing Satellite-2/Phased Array L-band Synthetic Aperture Radar-2 (ALOS-2/PALSAR-2) data across three Asian megacities (Tokyo, Bangkok, and Manila) and validated with Sentinel-2 land cover datasets. Results show that the refined POA-based decomposition significantly reduces misclassification, particularly between buildings and vegetation, compared with conventional approaches.

The novelty of this work lies in three main contributions. First, the method is fundamentally grounded in physical backscattering phenomena derived from controlled experimental data. Second, we demonstrate that a four-component decomposition provides a more physically consistent representation for classification compared to directly using the original scattering channels (HH, HV, VV). Third, we establish a methodological framework that successfully translates scattering physics from controlled experimental observations to large-scale satellite imagery, thereby addressing differences in scale and environmental complexity. The use of k-means clustering and Random Forest classifiers serves only as standard implementation tools rather than novel contributions.

The remainder of this paper is organized as follows. Section 2 introduces the datasets and study areas. Section 3 describes the polarimetric parameters employed. Section 4 details the proposed approach, including scattering decomposition, POA correction, and classification procedures. Section 5 presents experimental findings and evaluation. Section 6 summarizes key findings and outlines future research directions.

2. DATA

2.1 Satellite PolSAR Data: ALOS-2/PALSAR-2

Satellite-based Polarimetric Synthetic Aperture Radar (PolSAR) data were employed to support large-scale man-made structure classification. We utilized imagery from the Advanced Land Observing Satellite-2 (ALOS-2), equipped with the Phased Array type L-band Synthetic Aperture Radar-2 (PALSAR-2) sensor (JAXA, 2021a).

Operating at an L-band frequency of 1.27 GHz, the PALSAR-2 system offers strong penetration abilities and enhanced sensitivity to structural elements such as buildings, roads, and other urban features. Full polarimetric images, including HH (horizontal transmitting and horizontal receiving), HV (horizontal transmitting and vertical receiving), VH (vertical transmitting and horizontal receiving), and VV (vertical transmitting and vertical receiving) (JAXA, 2021b) were acquired over three major metropolitan regions (Tokyo, Bangkok, and Manila) between January and May 2024. The spatial resolution of the data is 6 meters in Stripmap mode, with off-nadir angles adjusted for optimal feature detection in each scene. The acquisition parameters for each city are summarized in Table 1.

Table 1. Details of PolSAR images used for the experiment.

City	Observation date	Off-nadir angle
Tokyo	2024-05-07	25.0°
Bangkok	2024-04-27	32.7°
Manila	2024-01-30	32.7°

The visual representation of these datasets is shown in Figure 1, where Red-Green-Blue (RGB) composites were generated by assigning Red, Green, and Blue to HH, HV, and VV, respectively. Figure 1(a) displays the PolSAR image of Tokyo, Figure 1(b) represents the Bangkok dataset, and Figure 1(c) shows the imagery for Manila. These images provide a foundation for testing the classification models under diverse urban morphologies and environmental conditions.

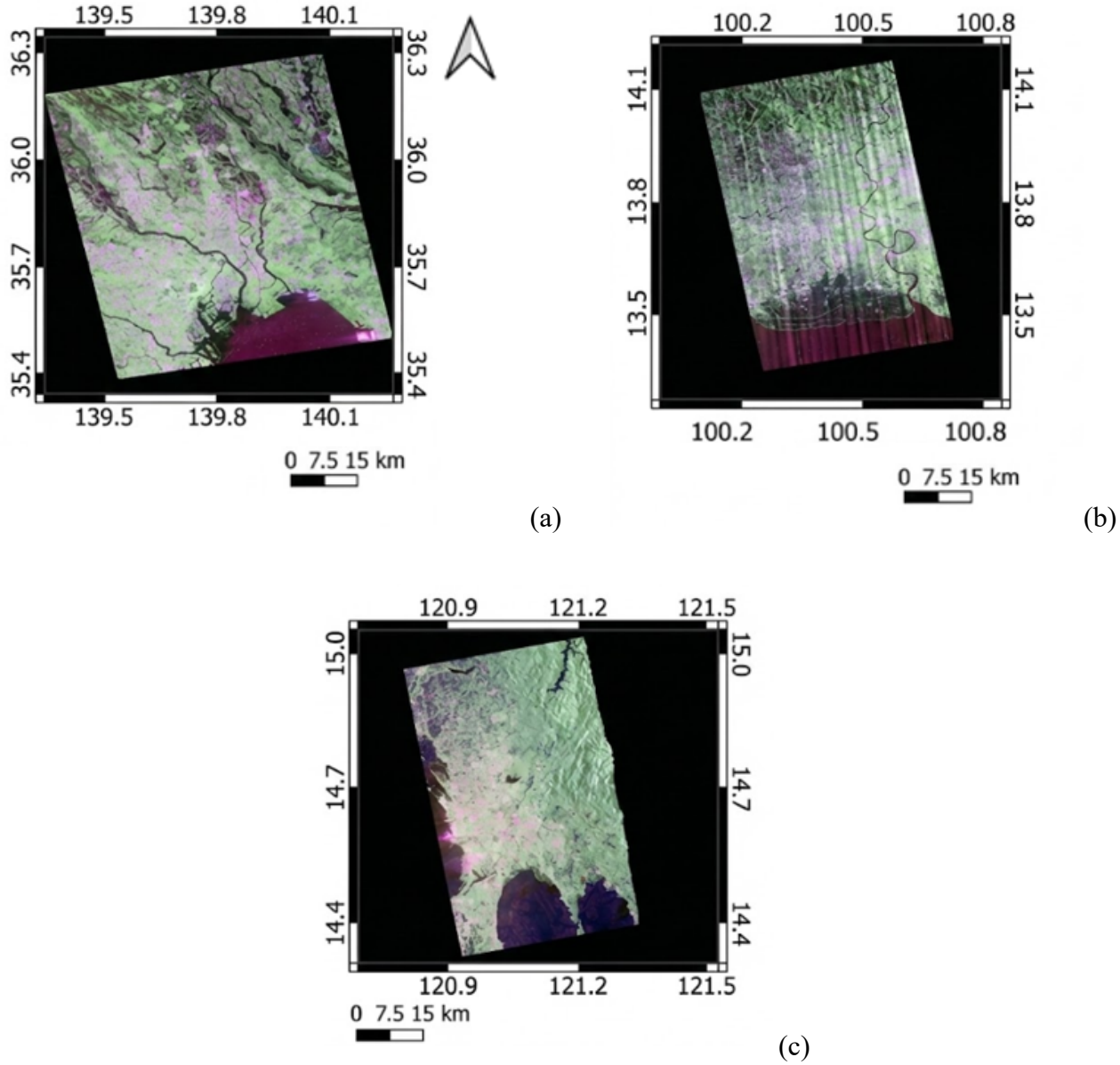

Figure 1. Polarimetric Synthetic Aperture Radar (PolSAR) images acquired with ALOS-2/PALSAR-2: (a) Tokyo (Red: HH, Green: HV, Blue: VV), (b) Bangkok (Red: HH, Green: HV, Blue: VV), and (c) Manila (Red: HH, Green: HV, Blue: VV).

As visible in Figure 1(b), the Bangkok image exhibits prominent vertical striping patterns in the RGB composite, which are characteristic of azimuth-direction noise or interference artifacts that can arise in L-band SAR acquisitions. No dedicated preprocessing was applied to suppress this striping prior to feature extraction, as the raw Level-1 data were used directly. However, this did not adversely affect the classification results. The striping artifacts are primarily manifested as intensity variations at the single-pixel level in the RGB visualization; once polarimetric decomposition features (Ps, Pd, Pv, Pc) are computed from the coherency matrix using spatial averaging (multilooking), and after the application of the majority filter in post-

processing, the influence of such localized noise is substantially reduced through spatial averaging and consensus-based smoothing. The strong classification accuracy achieved for Bangkok (OA = 95.5%) confirms that the artifacts did not degrade overall performance at the mapping scale of this study.

2.2 Experimental Reference Data: Microwave Scattering Measurements

To investigate the fundamental scattering behavior of man-made structures under controlled conditions, an experimental dataset comprising 37 measurements was obtained using microwave scattering measurements conducted in an anechoic chamber at Niigata University. The experiments were performed over two days from September 20 to 21, 2011. The setup utilized concrete block targets strategically positioned to simulate typical building structures, allowing for a controlled analysis of their polarimetric signatures across multiple azimuth angles (0°, ±5°, ±10°, ±15°, ±30°) to capture their orientation-dependent behavior comprehensively.

The measurements were conducted in the X-band frequency range (approximately 8 to 12 GHz, wavelength 3.8 to 2.5 cm) using a fully polarimetric radar system. The system acquired the complete scattering matrix, measuring the four complex polarizations: HH (horizontal-horizontal), HV (horizontal-vertical), VH (vertical-horizontal), and VV (vertical-vertical). This setup, repeated for each azimuth angle, provides a reference dataset for analyzing the polarimetric backscattering properties of rigid, man-made targets.

A clarification is needed regarding the polarization naming convention. In this experimental setup, the standard electrical engineering convention is used, where the first letter indicates the receive polarization and the second letter indicates the transmit polarization (Yamaguchi et al., 2018). This differs from the typical convention used in satellite-based radar remote sensing, where the order is often reversed (transmit first, then receive).

The configuration of the experimental setup, including target positioning and sensor orientation, is illustrated in Figure 2.

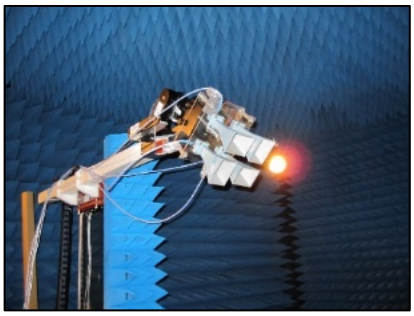

(a)

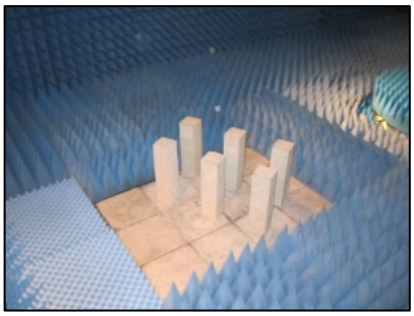

(b)

Figure 2. Setup of the microwave scattering measurement experiment in an anechoic chamber at Niigata University: (a) Sensor system measuring four polarizations (HH, HV, VH, and VV), and (b) Example of a concrete block used for the experiment.

This controlled dataset provides essential reference data for understanding fundamental scattering mechanisms of man-made targets. The use of calibrated targets in an anechoic chamber

ensures a clean separation of scattering mechanisms, free from environmental clutter, offering a reliable basis for developing classification algorithms.

2.3 Validation Data: Sentinel-2 Land Cover

For validation purposes, Sentinel-2 high-resolution land cover data for 2024 (Karra et al., 2021) were employed as reference data. These optical-derived land cover maps were resampled to match the 6-meter spatial resolution of the PALSAR-2 imagery. In this study, the Sentinel-2 land cover product is natively provided at 10 m spatial resolution and was resampled to 6 m using nearest-neighbor resampling, so that each 6 m PALSAR-2 pixel inherits the land cover label of the spatially closest Sentinel-2 pixel. High-density built-up areas are defined as pixels assigned the built-up label and located within large contiguous urban patches where the dominant surrounding land cover is also built-up. These correspond to dense urban blocks, commercial zones, and industrial facilities where double-bounce scattering from vertical structures is the dominant PolSAR response. Low-density built-up areas such as isolated buildings, sparse settlements, major roads, and open paved surfaces were excluded because these targets are typically sub-dominant scatterers at 6 m resolution and produce mixed or ambiguous PolSAR signatures that do not reliably generate the double-bounce response that the proposed method targets. Low-density classes such as major roads, open paved surfaces, and sparse settlements were intentionally excluded to minimize ambiguities and better isolate true man-made signatures. It is acknowledged that this focus on high-density areas may lead to optimistic accuracy estimates when the method is applied to broader urban mapping scenarios that include mixed or low-density built environments. The intended application scope of the proposed method is therefore primarily the detection and mapping of dense urban structures, and users should exercise caution when extending its use to peri-urban or low-density zones where scattering signatures are more ambiguous.

3. INDICES USED

3.1 Scattering Matrix (S)

The scattering matrix (S-matrix) describes the scattering behavior of a target and serves as the foundation for PolSAR data analysis (Lee and Pottier, 2009; Cloude and Pottier, 1996). It is commonly expressed as:

$$S = \begin{bmatrix} S_{HH} & S_{HV} \\ S_{VH} & S_{VV} \end{bmatrix} = \begin{bmatrix} a & c \\ c & b \end{bmatrix} \qquad (1)$$

Where S represents the complex scattering amplitude corresponding to different combinations of transmit and receive polarizations, with H and V denoting horizontal and vertical polarizations, respectively. Assuming that the target exhibits reciprocity, the scattering matrix satisfies the condition $S_{HV} = S_{VH}$.

3.2 Coherency Matrix (T)

The coherency matrix T, derived from the S-matrix, captures the power and correlation among polarization channels, providing a compact statistical description for decomposition techniques (Lee and Pottier, 2009; Cloude and Pottier, 1996). The 3×3 coherency matrix is given by:

$$T = \begin{bmatrix} T_{11} & T_{12} & T_{13} \\ T_{21} & T_{22} & T_{23} \\ T_{31} & T_{32} & T_{33} \end{bmatrix} = \frac{1}{2}\begin{bmatrix} |a+b|^2 & (a+b)(a-b)^* & 2(a+b)c^* \\ (a-b)(a+b)^* & |a-b|^2 & 2(a-b)c^* \\ 2c(a+b)^* & 2c(a-b)^* & 4|c|^2 \end{bmatrix} \quad (2)$$

The coherency matrix allows for eigen-decomposition and further physical interpretation of the scattering mechanisms.

3.3 Four-Component Decomposition

The four-component decomposition separates the total backscattered signal into surface (Ps), double-bounce (Pd), volume (Pv), and helix (Pc) scattering components (Yamaguchi et al., 2006), (Yamaguchi, 2020). To improve decomposition, the coherency matrix is rotated based on the estimated orientation angle:

$$T(\theta) = \begin{bmatrix} T_{11}(\theta) & T_{12}(\theta) & T_{13}(\theta) \\ T_{21}(\theta) & T_{22}(\theta) & T_{23}(\theta) \\ T_{31}(\theta) & T_{32}(\theta) & T_{33}(\theta) \end{bmatrix} =$$

$$[R_p(\theta)][T]\left[R_p(\theta)\right]^{\dagger} \quad (3)$$

Here, † indicates the operation of complex conjugation and transposition. Here, $R_p(\theta)$ is the rotation matrix defined as:

$$R_p(\theta) = \begin{bmatrix} 1 & 0 & 0 \\ 0 & cos2\theta & sin2\theta \\ 0 & -sin2\theta & cos2\theta \end{bmatrix} \quad (4)$$

This step reduces the effect of target misorientation and refines the scattering component estimation (Li et al., 2016).

3.4 Polarimetric Orientation Angle (POA)

POA quantifies the tilt of structures relative to the line of sight of the radar and is crucial for urban areas (Kimura, 2008; Li et al., 2016). POA is computed as:

$$\theta = \frac{1}{4}\tan^{-1}\left(\frac{2Re(\langle T_{23}\rangle)}{\langle T_{22}\rangle - \langle T_{33}\rangle}\right), \left(-\frac{\pi}{4} \le \theta \le \frac{\pi}{4}\right) \quad (5)$$

Incorporating POA improved classification performance by accounting for the geometric orientation of urban features (Kajimoto & Susaki, 2013).

3.5 Kullback-Leibler Divergence

The Kullback-Leibler (KL) Divergence measures the dissimilarity between probability distributions and is used to compare scattering behavior (especially Pd and Pv components) across different urban environments. Mathematically, the KL divergence from distributions (x) to $P(x)$ is defined as:

$$D_{KL}(P\|Q) = \sum_x P(x) log\left(\frac{P_{(x)}}{Q_{(x)}}\right) \quad (6)$$

Where $P(x)$ and $Q(x)$ represent the estimated probability densities of scattering values for a given land cover class in two different cities. A higher D_{KL} value indicates a greater divergence between the two distributions, revealing distinct differences in surface scattering behaviour that may impact classification.

In this study, Tokyo, Bangkok, and Manila are analyzed as representative urban areas to assess the variability in scattering behavior. High KL divergence values suggest significant differences in scattering characteristics between these cities, potentially affecting the classification of man-made structures.

3.6 Random Forest Classification and Regression

Random Forest (RF) is a supervised ensemble learning algorithm well-suited for high-dimensional PolSAR data because of its ability to

handle complex feature spaces, resist overfitting, and evaluate feature importance effectively (Breiman, 2001; Attri et al., 2024; Fang et al., 2018). Its strengths have made it a popular choice in urban land cover classification, particularly when used with polarimetric decomposition features and orientation information. Earlier studies demonstrated that combining decomposition parameters, such as those derived from the Yamaguchi four-component model, with POA enhances classification accuracy in urban areas (Hariharan et al., 2016; Zou et al., 2010). Building on this foundation, our proposed method further improves performance by integrating confidence-guided POA correction with an adaptive decomposition strategy and RF classification. This combination leverages the interpretability of physical scattering mechanisms, directional sensitivity of POA, and the robustness of ensemble learning, resulting in more reliable and accurate man-made structure extraction.

4. METHODOLOGY

4.1 Overview of the Proposed Method

Our method presents a comprehensive framework for extracting man-made structures from PolSAR data by integrating experimental backscattering understanding, satellite imagery, decomposition features, and machine learning. As shown in the conceptual flowchart (Figure 3), the workflow consists of six major stages: (1) data collection, (2) input and preprocessing, (3) machine learning, (4) three-step refinement, (5) feature refinement, and (6) final classification and output.

Stage 1: Data Collection incorporates two sources: experimental PolSAR data and satellite-based observations. The experimental dataset was acquired through controlled measurements using concrete blocks within an anechoic chamber to characterize fundamental scattering behaviour of man-made structures. Simultaneously, full-polarimetric ALOS-2/PALSAR-2 satellite imagery of urban regions was used to capture the large-scale backscattering characteristics of real-world urban environments.

Stage 2: Input and Pre-processing focuses on both feature extraction and data integration. Feature extraction is performed using a modified Yamaguchi four-component decomposition method, which separates the polarimetric data into Ps, Pd, Pv, and Pc scattering components. Additionally, POA is estimated and incorporated as an essential feature to enhance the detection of structural orientation. In parallel, a data integration step is performed by applying k-means clustering to the HH, HV, and VV channels of the experimental dataset. This partitions the data into man-made and non-man-made categories based on their scattering characteristics, allowing for a labeled dataset serving as a reliable reference for classifier training.

Stage 3: Machine Learning employs the labeled experimental data to train a classifier that is then applied to the satellite-derived features. The learning process benefits from the inclusion of both POA and decomposition features, allowing the model to differentiate between subtle variations in scattering responses across urban and natural landscapes.

Stage 4: Three-Step Refinement enhances classification accuracy through: (a) POA correction using a confidence-based approach to

stabilize orientation estimates, particularly in regions with ambiguous or noisy scattering responses; (b) adaptive scattering decomposition that modifies the Yamaguchi model by redistributing scattering power to emphasize differences between man-made and natural features, thereby reducing misclassification in mixed scattering zones; and (c) statistical adjustment conducted using region of interest (ROI) analysis, where class-specific statistics are derived from selected land cover type samples.

Stage 5: Feature Refinement integrates the corrected POA and enhanced decomposition features to generate final class probabilities, ensuring that all corrections and enhancements are effectively captured before the classification stage.

Stage 6: Classification and Output uses the refined features to produce a classification map, with a focus on accurately extracting man-made structures. A majority filtering step is implemented using a circular neighborhood with a 10-pixel radius (equivalent to a ~60 m radius or ~120 m diameter at 6 m spatial resolution) to eliminate isolated misclassified pixels and improve the spatial coherence of the output map. It should be noted that this filter footprint is substantial and may smooth fine-grained boundaries between urban and non-urban areas; users requiring sub-block spatial precision should consider reducing the filter radius or omitting this step.

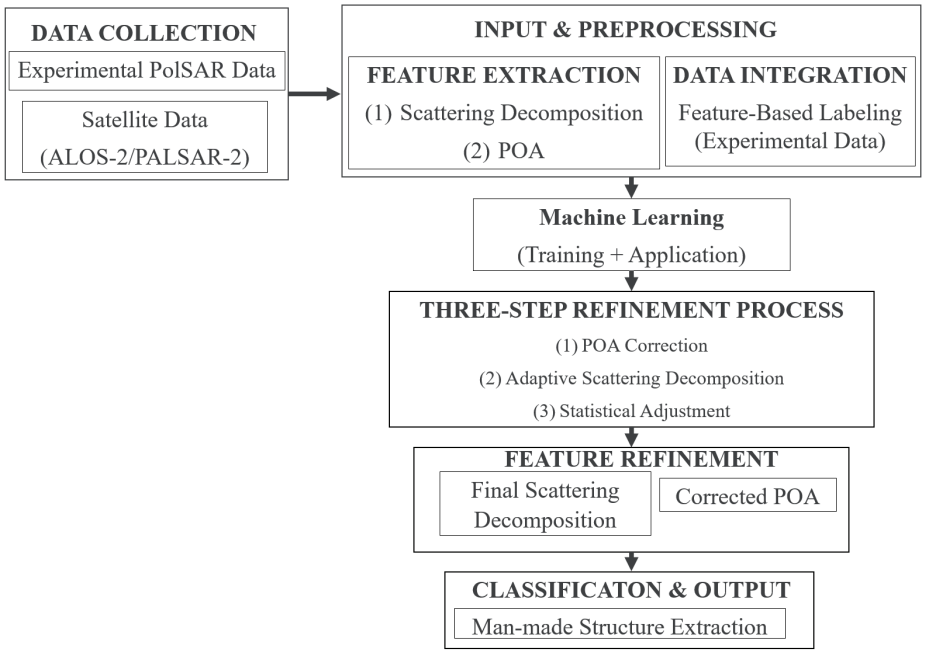

Figure 3. Overview of the proposed method for man-made structure extraction using PolSAR data.

4.2 Training Dataset Preparation

We developed a training dataset using the PolSAR backscattering data from the 37 controlled experiments described in Section 2.2. A critical methodological consideration arises from the frequency difference between experimental data (X-band, 8–12 GHz, collected in 2011) and satellite applications (L-band, 1.27 GHz, acquired in 2024).

The validity of transferring scattering knowledge from X-band experiments to L-band satellite data rests on three principles. First, fundamental scattering mechanisms remain frequency-invariant for targets larger than the wavelength. Double-bounce scattering from ground-wall interactions produces a dominant Pd component in both frequency bands, though absolute backscatter magnitudes differ (Lee and Pottier, 2009; Yamaguchi et al., 2011). Second, the Random Forest classifier learns relative relationships between scattering components (e.g., Pd/Pv ratios) rather than absolute backscatter values, making it robust to frequency-dependent scaling (Breiman, 2001). The decision boundaries are determined by feature space topology, which remains physically consistent across frequencies. Third, the dielectric properties of concrete ($\varepsilon r \approx 5$–7) and geometric characteristics are time-invariant, making the 13-year temporal gap between experiments and satellite acquisition negligible.

To mitigate potential frequency-dependent biases, two safeguards were implemented: (1) confidence-based POA correction (Section 4.3) adapts to orientation-dependent scattering variations specific to L-band data, and (2) ROI-based statistical refinement (Section 4.5) recalibrates decomposition parameters using statistics derived directly from L-band satellite imagery (Equation 13). This two-stage adaptation ensures that the X-band-trained model generalizes effectively to L-band observations. Previous studies have validated cross-frequency transfer for PolSAR urban classification, demonstrating that decomposition-based features maintain structural consistency from C-band to L-band when models are trained on fundamental scattering mechanisms (Singh et al., 2013; Hariharan et al., 2016).

As the experimental dataset lacked predefined class labels, k-means clustering (k = 2) was applied to the HH, HV, and VV backscatter intensity values, partitioning the data into man-made (concrete blocks, label = 1) and non-man-made (anechoic chamber background, label = 0) classes. This unsupervised approach identifies class boundaries based on statistical separability in the polarimetric feature space.

The final dataset comprises approximately 600,000 pixels extracted from concrete block areas across all 37 experiments, covering azimuth angles of 0°, ±5°, ±10°, ±15°, and ±30°. These pixels serve as input for the Random Forest classifier, using eight explanatory variables:

$$X = [HH, HV, VV, Ps, Pd, Pv, Pc, POA] \quad (7)$$

Where HH, HV, VV represent backscatter intensities (linear power units), Ps, Pd, Pv, Pc are Yamaguchi decomposition components, and POA is the polarimetric orientation angle. The Random Forest algorithm evaluates feature importance non-parametrically through decision tree partitioning, making it inherently robust to scaling differences between X-band and L-band data.

Figures 4a–4c show dB-scaled backscatter distributions for each polarization, demonstrating bimodal separation between classes. Figure 4d presents classification results from Experiment 17 (30° azimuth), illustrating angular dependence of scattering behaviour. It is noted that the POA in urban areas is influenced not only by building orientation but also by radar incidence angle and local scattering geometry. In this study, the use of multiple azimuth angles in the training data

captures general orientation-related scattering variability rather than directly representing building orientation, thereby improving classifier robustness when applied to satellite imagery.

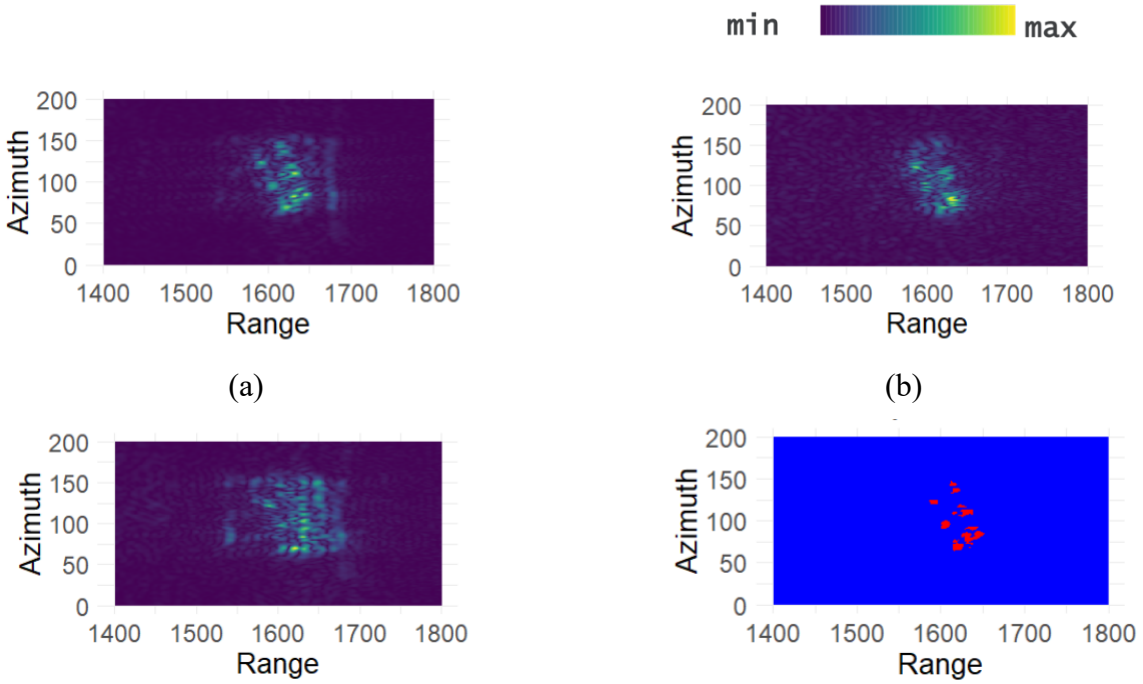

Figure 4. X-band scattering experiment clustering results for man-made structure classification (experiment 17, 30° orientation Angle): (a) HH, (b) HV, (c) VV, and (d) classification (red: man-made, blue: non-man-made).

4.3 POA Estimation and Confidence-Based Correction

Accurate extraction of man-made features using polarimetric SAR data is often challenged by orientation-induced distortions, particularly in complex urban environments where buildings and man-made structures are not always aligned with the radar line of sight. These orientation variations can significantly affect the accuracy of POA estimation, leading to classification errors, especially in boundary regions where scattering characteristics of man-made and natural areas overlap.

Accordingly, we introduced a confidence-based POA correction framework. The purpose of this framework is to prioritize areas with strong and stable backscattering responses while down-weighting regions with weak or ambiguous scattering.

In practice, POA estimation is influenced by factors such as speckle noise, image resolution, and urban infrastructure variability. Figure 5 illustrates the impact of these factors using experimental dataset 13, where the orientation angle was set to 10 degrees. In Figure 5a, the estimated POA plot shows a mean value of 12.42 degrees within the red rectangle, highlighting a discrepancy of 2.42 degrees from the expected 10 degrees. Figure 5b presents the residual plot, displaying the difference between the actual and estimated POA values (Actual POA - Estimated POA). These results indicate that the current

estimation method does not adequately capture the intended orientation angle, especially in regions with strong backscattering. This underlines the need for a more robust POA correction mechanism to mitigate misclassification in complex urban environments.

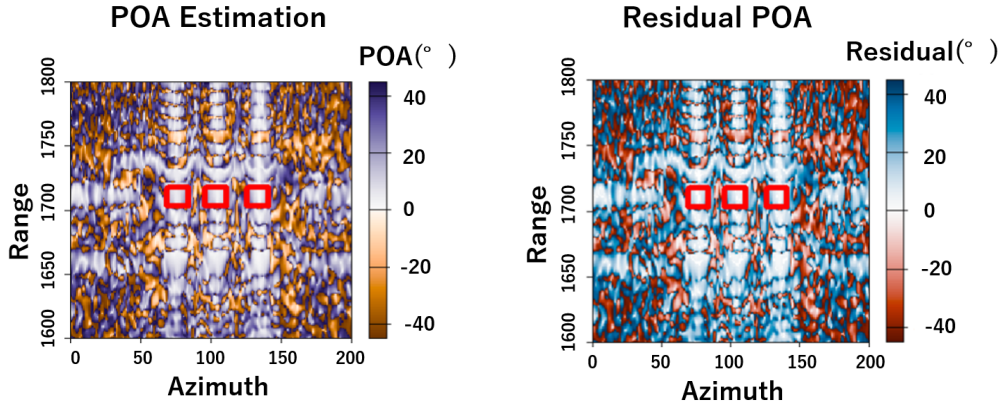

(a) (b)

Figure 5. Polarimetric orientation angle (POA) estimation analysis and residuals in the experimental dataset (experiment 13, 10° orientation angle): (a) Estimated POA distribution with the concrete block location highlighted by the red rectangle, where the expected and the mean estimated POAs are 10° and 12.42°, respectively. (b) Residual POA plot showing the difference between the actual (10°) and estimated POAs. The concrete block has a size of 10 cm × 10 cm × 40 cm, and the red rectangle is equivalent to an area of 10 cm × 10 cm.

To improve the reliability of POA estimates, we developed a comprehensive confidence prediction model using the experimental dataset. This controlled dataset served as a benchmark for quantifying estimation errors and refining our correction strategy. The methodology begins with calculating the Weighted Residual Sum of Squares (WRSS) to evaluate discrepancies between the actual and estimated POA responses.

$$WRSS = \sum_{i=1}^{n} w_i v_i^2 \qquad (8)$$

In this formulation, n represents the total number of observations or pixel samples considered in the analysis. Each observation is assigned a weight (w_i) based on its backscatter intensity, calculated as the total power across all three polarizations (HH, HV, VV). This approach emphasizes areas with stronger backscatter signals, allowing them to exert greater influence in the POA correction process. The residual (v_i) quantifies the discrepancy between the actual and estimated POA responses, serving as a crucial indicator of estimation reliability.

From the WRSS, we derive a normalized confidence score (C_s) quantifying the reliability of each POA estimate:

$$C_s = \frac{WRSS}{max(WRSS)} \qquad (9)$$

Where *max(WRSS)* represents the maximum WRSS value observed in the dataset. This score ranges from 0 to 1, with higher values indicating greater confidence in the estimate.

Building on this foundation, we compute the refined POA(θ') through an innovative weighted combination:

$$\theta' = C_s \cdot \theta_{POA} + (1 - C_s) \cdot \sigma_{POA} \quad (10)$$

Where θ_{POA} and σ_{POA} are the original POA estimate and local POA standard deviation, respectively. For example, consider an initial POA estimate of 20° with a local standard deviation of 18° and a confidence score of 0.8. The refined POA would be calculated as (0.8 × 20°) + (0.2 × 18°) = 19.6°. The refinement process effectively bridges the gap between point estimates and regional scattering behaviour, yielding more accurate and representative POA values across diverse terrain conditions.

4.4 Adaptive Scattering Decomposition

In addition to the POA correction, scattering decomposition was employed to separate the total backscattered signal into surface, double-bounce, and volume scattering components. These decomposition-based features were then used as inputs to the Random Forest classifier to enhance classification accuracy, especially in complex urban areas where overlapping scattering mechanisms often lead to misclassification.

All scattering powers used here were recalculated from the decibel (dB) scale to linear ratio form using the standard conversion: $Power_{ratio} = 10^{(\frac{Power_{dB}}{10})}$. This transformation was essential to ensure consistent interpretation and computational stability during feature extraction and classification.

In urban environments, orientation misalignment can cause scattering ambiguity. For instance, double-bounce returns from vertical structures such as building walls may resemble volume scattering if the structure is rotated relative to the radar. This is a common challenge in existing scattering decomposition methods, which often struggle to effectively distinguish buildings with different orientation angles from forests.

The modified Yamaguchi decomposition employed in this study addresses this challenge through an adaptive power redistribution scheme. Building upon the standard four-component model, our approach incorporates the refined orientation angle ((θ')) to dynamically adjust the separation between double-bounce and volume scattering components. This is achieved through the following correction equations:

$$P_d^{corr} = cos^2(2\theta')P_d + sin^2(2\theta')P_v + \sin(2\theta')\cos(2\theta')(P_d - P_v) \quad (11a)$$

$$P_v^{corr} = sin^2(2\theta')P_d + cos^2(2\theta')P_v - \sin(2\theta')\cos(2\theta')(P_d - P_v) \quad (11b)$$

These equations are derived from the rotation matrix (R_p) and the scattering matrix transformation S(ξ), which aligns the scattering components with the true orientation of the target. The rotation matrix (R_p) is expressed as shown in Equation (4).

The cross-term $(P_d - P_v)\sin(2\theta')\cos(2\theta')$ arises directly from this rotation process. It reflects the coupling between the double-bounce and volume scattering mechanisms when the scene is rotated relative to the radar line of sight. In other words, the power from these two mechanisms is not independent under rotation: part of the double-bounce contribution can be redistributed into volume scattering and vice versa, depending on the orientation angle. This coupling ensures that the corrected powers (P_d^{corr}, P_v^{corr}) properly represent the physical scattering mechanisms aligned with the actual target orientation, thereby reducing

misclassification in urban areas where orientation effects are significant.

The explanatory variables in this study were not used simultaneously in a single feature set but were instead evaluated through four separate experimental scenarios. In the first scenario, only the original backscatter channels (HH, HV, VV) were employed to assess the role of direct polarization-dependent intensity. The second scenario relied solely on decomposition parameters (Ps, Pd, Pv, Pc), which represent distinct physical scattering mechanisms. The third scenario combined decomposition parameters with POA correction, while the fourth scenario further refined decomposition by explicitly incorporating POA. This design enabled a systematic comparison of different representations of PolSAR data, ensuring that redundancy was avoided and allowing us to highlight the additional contribution of POA-based corrections in improving urban classification.

4.5 Refinement Using ROI Statistics

A primary challenge in distinguishing man-made structures from natural areas using polarimetric SAR data is the overlapping scattering characteristics, particularly between Pd and Pv. Built-up areas typically exhibit strong Pd signals from vertical structures, while forested areas generate Pv because of canopy scattering. However, similar scattering responses in these contexts can lead to confusion between vegetation and man-made structures.

To enhance the accuracy of scattering decomposition and improve the discrimination of man-made structures, a ROI analysis was conducted across five representative land cover classes: agriculture, water, bare land, forest, and man-made areas. For each class, between 10 and 15 samples were carefully selected using uniformly sized 50 m² grid cells to ensure consistent spatial representation.

In Figure 6, the density plots are generated using kernel density estimation (KDE), which provides a smoothed curve rather than a discrete histogram. This approach highlights the distributional patterns of the scattering components across classes, allowing for a clearer visualization of Pd and Pv variations. Unlike histograms displaying frequency counts, KDE offers a continuous density representation, revealing subtle differences in scattering behaviours even when the number of pixels is consistent across classes.

The Pd and Pv ranges differ significantly across classes, indicating that while some classes exhibit low scattering power (e.g., water), others, like man-made structure areas, display higher scattering power because of stronger backscatter returns. This distinction is crucial for refining the decomposition analysis and improving classification accuracy.

From these ROIs, statistical metrics were extracted for all four scattering components: Ps, Pd, Pv, and Pc. The extracted features included the mean, standard deviation, skewness, and kurtosis, providing detailed insights into the distributional characteristics and variability of each scattering type across different land covers.

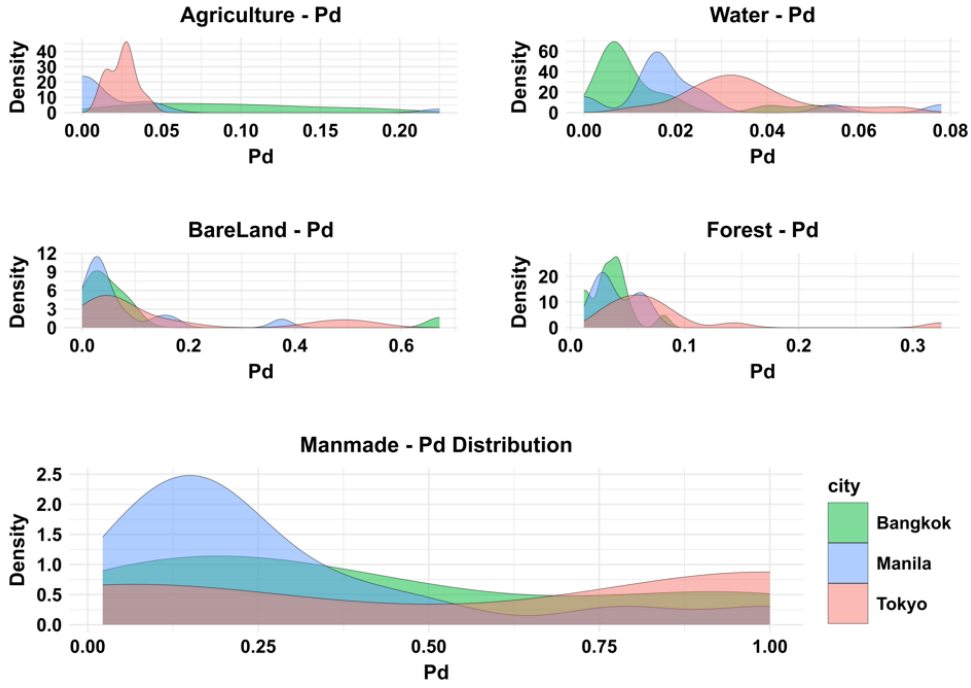

(a)

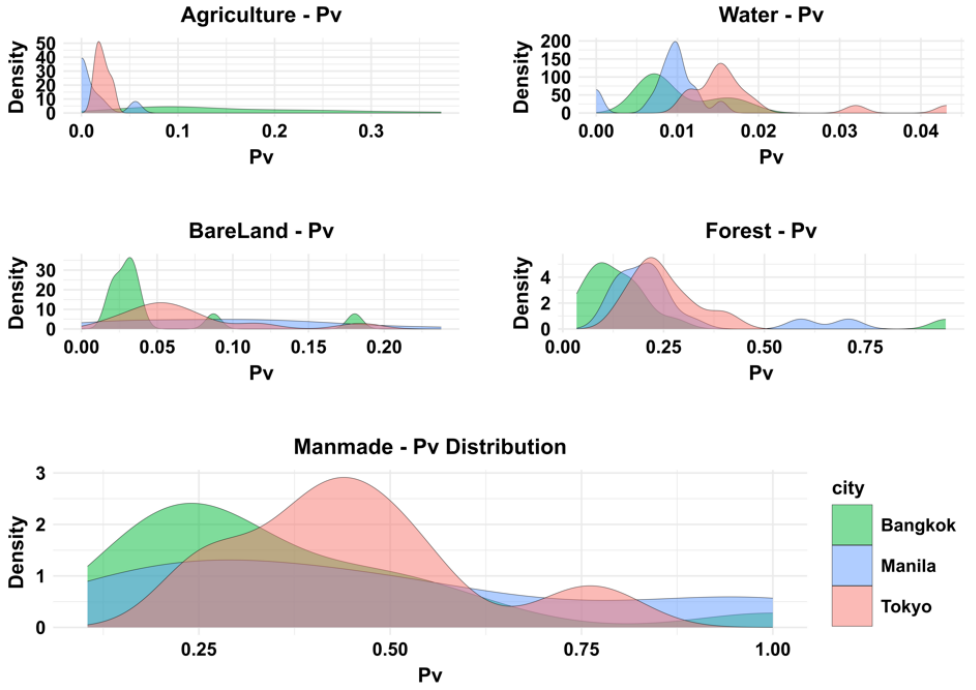

(b)

Figure 6. Spatial distribution of ROI samples for five major land cover classes: (a) Pd density distributions across land cover types, and (b) Pv density distributions across land cover types. The density distributions are generated using kernel density estimation (KDE) to provide a continuous representation of the scattering characteristics across each class.

To improve class separability, the decomposition components were transformed according to their statistical distinctiveness within training regions. Instead of relying on raw powers, we introduced a normalized likelihood ratio for each component to enhance the contrast between target and non-target classes. For the double-bounce component, the refinement was expressed as:

$$\boldsymbol{Pd_{refined} = Pd \times \frac{\mu_{d,man-made\ structure}}{\mu_{d,non-man-made\ structure}}} \quad (13)$$

Where $\mu_{d,man-made\ structure}$ is the mean Pd within man-made structure ROIs and $\mu_{d,non-man-made\ structure}$ is the mean over all other land-cover classes. This ratio exceeds 1 in man-made structure areas and falls below 1 elsewhere, thereby amplifying the double-bounce signal in regions where it is statistically dominant. Conceptually, the ratio functions as a physical likelihood measure: values above unity indicate a higher probability of man-made structure scattering behaviour, while values below unity indicate the opposite. The same normalization strategy was applied to Ps (emphasizing bare soil and water surfaces) and Pv (emphasizing vegetation), ensuring a balanced refinement across all scattering processes.

Thereafter, outlier suppression was implemented by clipping values exceeding a statistical threshold defined by the mean and standard deviation of the component. Specifically, values greater than $Pd_{mean} + Pd_{sd}$ were capped, thereby mitigating the influence of anomalous pixels that may otherwise skew the classification. In cases where the component distributions exhibited strong positive skewness (greater than 1), a logarithmic transformation was applied to normalize the values and reduce the impact of extreme tails. This transformation was expressed as: $Pd_{refined} = \log(Pd + 1)$. Such statistical normalization techniques were particularly effective in addressing uneven brightness responses and enhancing the stability of classification across heterogeneous urban environments.

The impact of this refinement process is clearly illustrated in Figure 7, which compares the original and refined decomposition results for the Tokyo metropolitan area. The zoomed-in insets focus on three iconic urban green spaces: Meiji Jingu Gyoen, Shinjuku Gyoen Garden, and Motoakasaka. Before refinement, the Pv component (Pv–green) appeared subdued in these densely vegetated areas, which limited the visibility and detectability of natural vegetation. After applying the refinements, Pv signals became significantly more prominent, enabling clearer recognition of vegetated zones. Simultaneously, the Pd scattering (Pd–red) became more sharply defined around nearby buildings and infrastructure, increasing contrast between built and natural environments and improving the segmentation of man-made features.

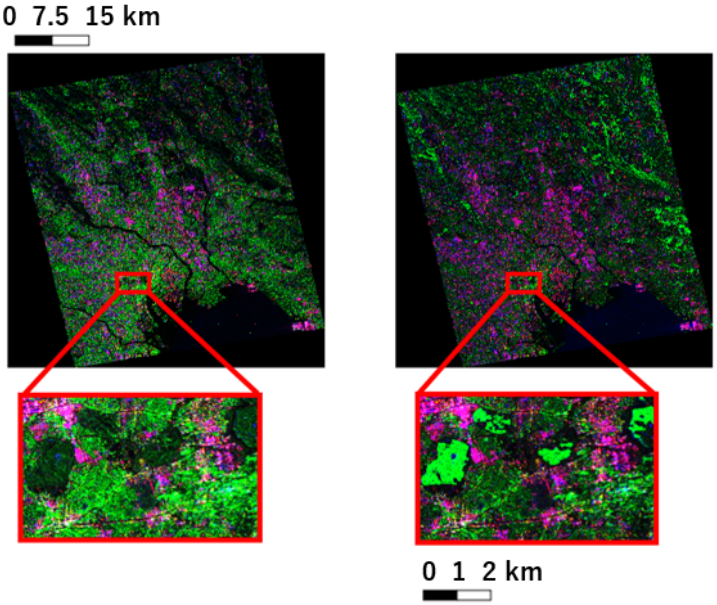

Figure 7. Scattering decomposition before and after refinement in the Tokyo metropolitan area. Insets highlight changes in Meiji Jingu Gyoen, Shinjuku Gyoen Garden, and Motoakasaka, showing enhanced representation of Pd (Pd–red) in built-up areas and improved Pv (Pv–green) in vegetated zones. Surface scattering (Ps–blue) remains prominent in bare or flat surfaces: (a: left) and (b: right) illustrate before and after refinement, respectively.

To assess the generalizability of this approach, Figure 8 presents additional results from Bangkok and Manila, illustrating the decomposition before and after refinement. Although zoomed-in insets are not provided for these cities, the global changes are still evident: enhanced Pd (red) responses in built-up districts and clearer Pv (green) representation in vegetated or less-developed areas are consistently observed. These outcomes reinforce the adaptability of the ROI-based refinement method across diverse urban landscapes, including cities with varying levels of density, vegetation coverage, and architectural patterns.

By integrating statistically based refinements with physical scattering interpretations, this approach strengthens the capability of polarimetric SAR decomposition in delineating complex urban scenes. The enhanced representation of Ps, Pd, and Pv enables more robust classification frameworks and better supports urban mapping efforts across heterogeneous metropolitan regions.

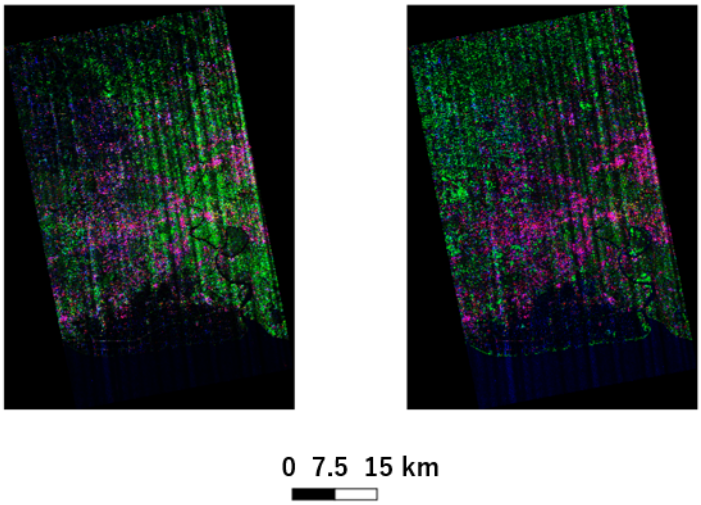

(a) (b)

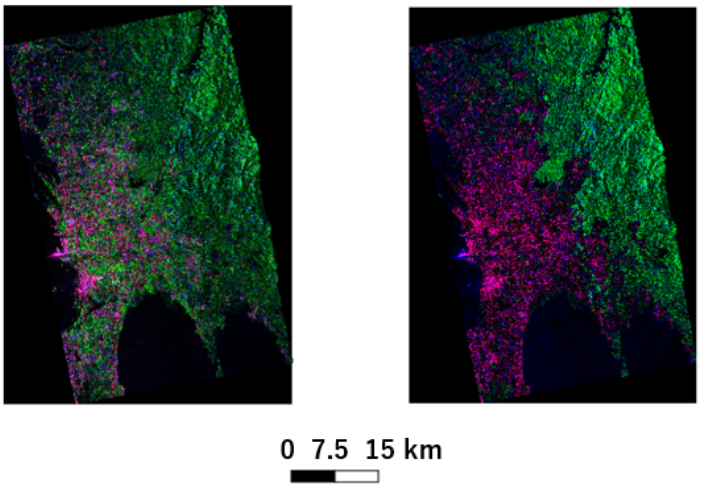

(c) (d)

Figure 8. Comparison of original and refined scattering decomposition in Bangkok and Manila. The refinement process enhances Pd responses (Pd–red) in dense urban areas and improves Pv (Pv–green) visibility in forested or vegetated zones. The refined decomposition also maintains strong Ps (Ps–blue) patterns in open land areas: (a) and (b) represent before and after refinement in Bangkok, respectively, and (c) and (d) illustrate before and after refinement in Manila, respectively.

4.6 Hyperparameter Tuning and Validation

To classify man-made and non-man-made structures, an RF classifier was employed, leveraging the corrected scattering components, specifically the refined Pd and Pv powers ($Pd_{refined}$, $Pv_{refined}$) alongside other polarimetric features derived from the PolSAR dataset. These corrected components were calculated based on the proposed scattering decomposition refinement approach, ensuring better alignment with actual surface orientations and reducing classification errors because of misinterpreted scattering mechanisms.

Hyperparameter optimization for the RF model was performed using a random search strategy, a computationally efficient method for

exploring parameter space. The optimal configuration determined from this process set mtry = 2, indicating that two variables were randomly selected at each node split, and ntree = 100, specifying the use of 100 decision trees to construct the ensemble model. This tuning aimed to balance classification performance with computational efficiency, preventing overfitting while maintaining generalization across urban types.

For model validation, Sentinel-2 land cover data were employed as reference, resampled to match the 6 m spatial resolution of the PALSAR-2 imagery. Validation focused specifically on high-density built-up areas to ensure that the classification model targeted structurally significant man-made features. Low-density classes such as major roads, open paved surfaces, and sparse settlements were intentionally excluded to minimize ambiguities and better isolate true man-made signatures.

The combined use of POA correction, enhanced scattering decomposition features, and high-resolution PolSAR imagery provided a robust framework for evaluating the performance of the classifier. The results demonstrated the ability of the model to accurately discriminate man-made structures across diverse urban environments, confirming the effectiveness of the proposed method for large-scale man-made feature extraction from PolSAR data.

5. RESULTS AND DISCUSSION

The proposed classification approach was validated using Sentinel-2 high-resolution land cover data for 2024 (Karra et al., 2021). The exclusion of ground-level features improved accuracy in identifying elevated man-made structures.

5.1 Quantitative Assessment

The classification approach was evaluated across Tokyo, Bangkok, and Manila to extract vertical man-made structures while excluding flat surfaces. During post-processing, we applied a 10-pixel radius circular neighborhood filter with a 25% classification agreement threshold. The role of this filter in the reported accuracy is discussed below.

Regarding the influence of the majority filter on reported accuracy, it is important to note that the substantial accuracy gains observed in this study, ranging from 15 to 20 percentage points over the baseline, are driven by the progressive improvements from scattering decomposition, POA correction, and adaptive refinement, as shown by the step-by-step accuracy progression reported in Figures 9–11. We acknowledge that the same majority filter was applied uniformly across all four processing stages shown in those figures, meaning the filter itself is not the source of the cross-stage improvements; rather, the gains arise from each successive enhancement to the physical processing pipeline. The majority filter was applied as a final noise-reduction step to remove isolated misclassified pixels, predominantly single-pixel or small-cluster artifacts in scattering transition zones, and to improve the visual and spatial coherence of the output map. Its contribution to overall accuracy is therefore expected to be modest; pixels corrected by the filter are those surrounded by a strong spatial consensus of the opposite class, meaning they were already likely misclassifications rather than structurally meaningful detections. We

acknowledge that the ~120 m filter diameter represents a significant spatial footprint, and in areas with fine-grained urban-vegetation interfaces, some boundary pixels may have been reassigned. Users applying this method in contexts requiring sub-block spatial precision should consider reducing the filter radius or omitting this step entirely.

In Tokyo, the overall accuracy (OA) increased from 79.2% to 87.0% after applying scattering decomposition. Incorporating the POA further raised the OA to 90.4%, and the refined decomposition method, including the impact of POA correction and refined scattering decomposition, achieved the highest accuracy of 94.4%.

In Bangkok, the OA progressed from 83.6% to 86.3% after decomposition, then to 92.4% after incorporating POA, and peaked at 95.5% following the refining step.

Similarly, in Manila, the OA increased from 85.8% to 87.6% after decomposition, then to 92.1% with POA integration, and reached 95.6% after POA correction and scattering decomposition refining.

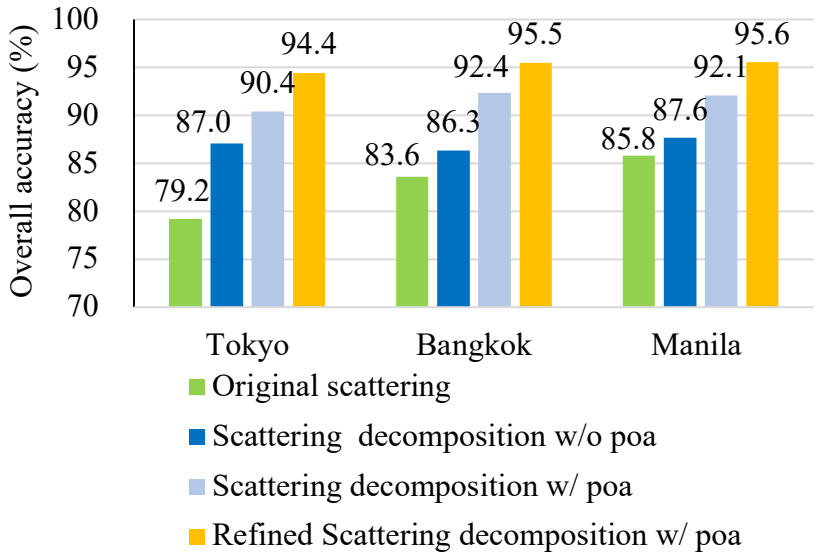

Figure 9. Overall accuracy (OA) for man-made structure classification in Tokyo, Bangkok, and Manila across four processing stages: original backscatter channels, scattering decomposition, decomposition with POA, and refined decomposition.

While the primary objective was to exclude flat surfaces, the filtering step led to the inclusion of main roads because of pixel merging. Nevertheless, this adjustment resulted in a more spatially coherent classification output, effectively balancing noise reduction and structural integrity in complex urban environments.

In addition to overall accuracy, the Producer's Accuracy (PA) and User's Accuracy (UA) were also evaluated to assess the classification performance more comprehensively. As shown in Figure 10, PA exhibited significant improvements across all cities with each enhancement stage. In Tokyo, PA improved from 73.9% (original) to 87.3% (decomposition), then to 88.4% after POA inclusion, and rose sharply to 94.5% with

refinement. Bangkok displayed a strong upward trend in PA from 84.0% to 86.0%, followed by 92.2%, and finally 95.5%. Manila demonstrated the highest PA performance, progressing from 88.6% to 89.8%, then to 93.2%, and reaching 96.3% with the refined method. These results indicate a consistent reduction in omission errors, especially after the application of POA and refinement procedures.

UA, as illustrated in Figure 11, also improved significantly across all cities. In Tokyo, UA increased from 78.0% (original) to 80.5% (decomposition), further rose to 90.8% (with POA), and slightly improved to 91.0% after refinement. Bangkok recorded an impressive UA increase from 78.6% to 88.6%, then to 94.0%, and reached 95.5%. In Manila, UA steadily increased from 88.4% to 89.4%, followed by 93.5%, and finally reached 94.7%. These results reflect a significant reduction in commission errors, particularly after incorporating POA into the classification process.

The observed classification improvements are not solely attributed to enhanced scattering analysis. Scene-specific factors such as the incidence angle of the satellite also influence classification performance. Variations in incidence angles affect the interaction of electromagnetic waves with urban surfaces, potentially altering backscattering characteristics. This effect partly explains the variability in performance across cities and reinforces the importance of scene-adaptive processing techniques.

Overall, the combined use of POA correction and refinement via region-based filtering led to considerable gains in all evaluated metrics OA, PA, and UA across all three urban environments. The classification framework proved especially effective in minimizing both omission and commission errors, thereby enhancing the consistency and interpretability of the results.

Among the three cities, Bangkok showed the greatest relative improvement, with OA increasing from 83.6% to 95.5%, PA from 84.0% to 95.5%, and UA from 78.6% to 95.5%. This highlights the important role of POA correction and spatial refinement in complex urban landscapes where structural heterogeneity and orientation effects are pronounced. Additionally, Figure 12 displays the classification results for Tokyo, Bangkok, and Manila using the refined scattering decomposition with POA

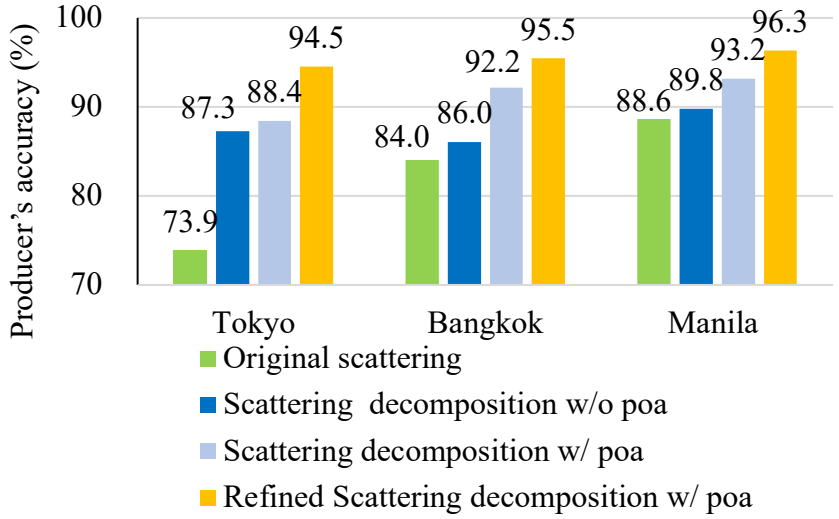

Figure 10. Producer's accuracy (PA) for man-made structure classification in Tokyo, Bangkok, and Manila across four processing stages.

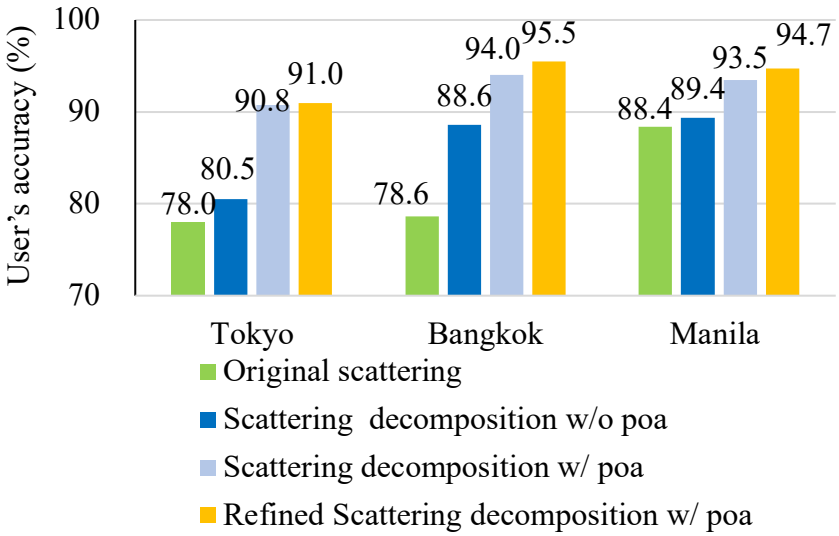

Figure 11. User's accuracy (UA) for man-made structure classification in Tokyo, Bangkok, and Manila across four processing stages.

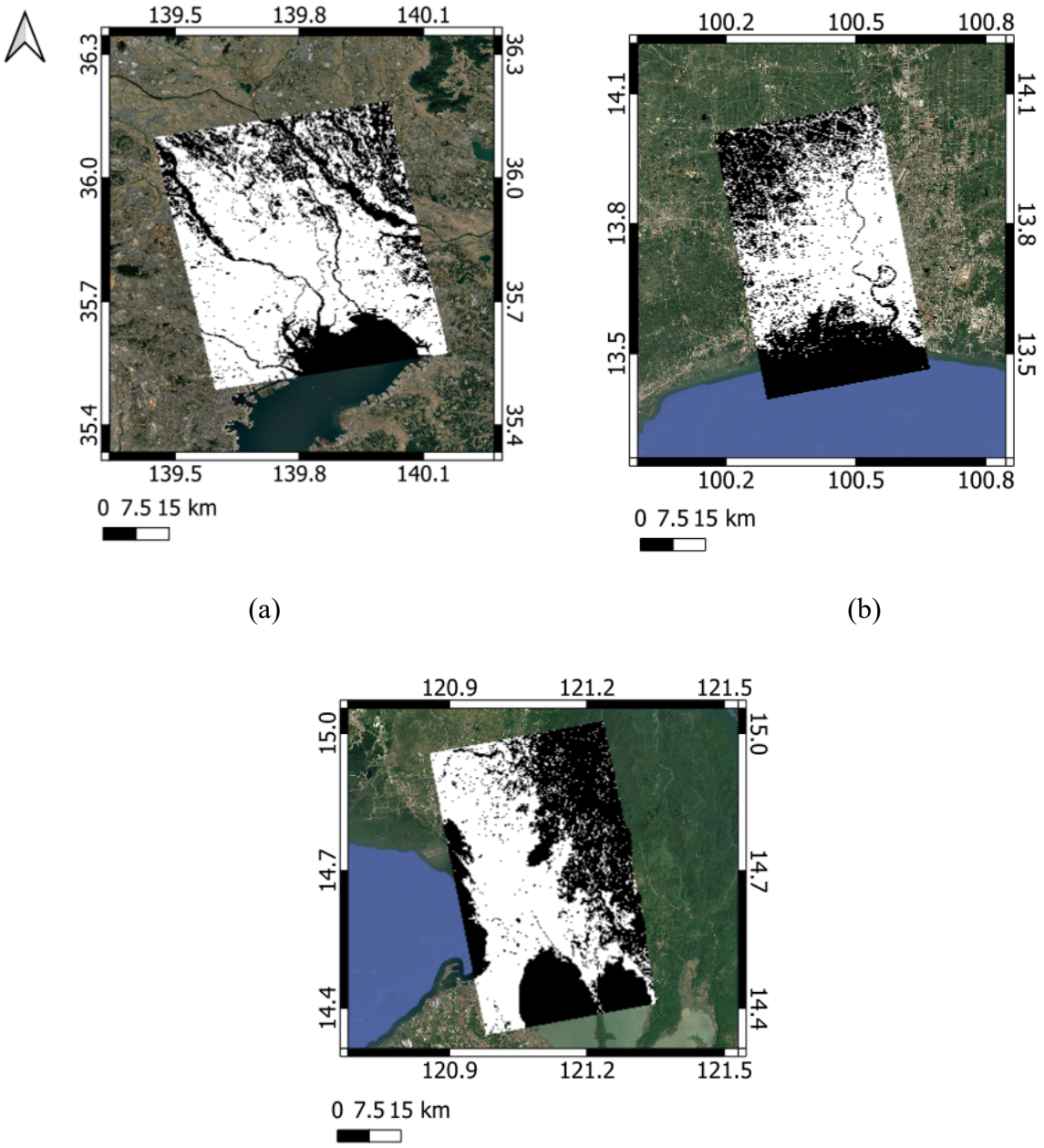

Figure 12. Classification results using refined scattering decomposition with POA: (a) Tokyo, (b) Bangkok, and (c) Manila. White indicates man-made structures; black indicates non-man-made areas.

5.2 Comparative Analysis of Methods

The proposed method significantly reduces the misclassification of vegetated areas (e.g., parks, golf courses) as man-made structures, a major source of error in the baseline Yamaguchi decomposition. This improvement is achieved by integrating scattering decomposition, POA correction, and a final refinement step to differentiate overlapping scattering characteristics.

As shown in Figure 13, the refined decomposition (right column) corrects the widespread errors of the traditional method (middle column), achieving strong agreement

with the Sentinel-2 reference data (left column). The red circles highlight specific locations, such as golf courses, where volume scattering from vegetation was previously confused for the double-bounce scattering of buildings.

These results demonstrate the method's robustness in diverse urban environments, effectively minimizing both false positives in natural areas and the omission of true built-up structures.

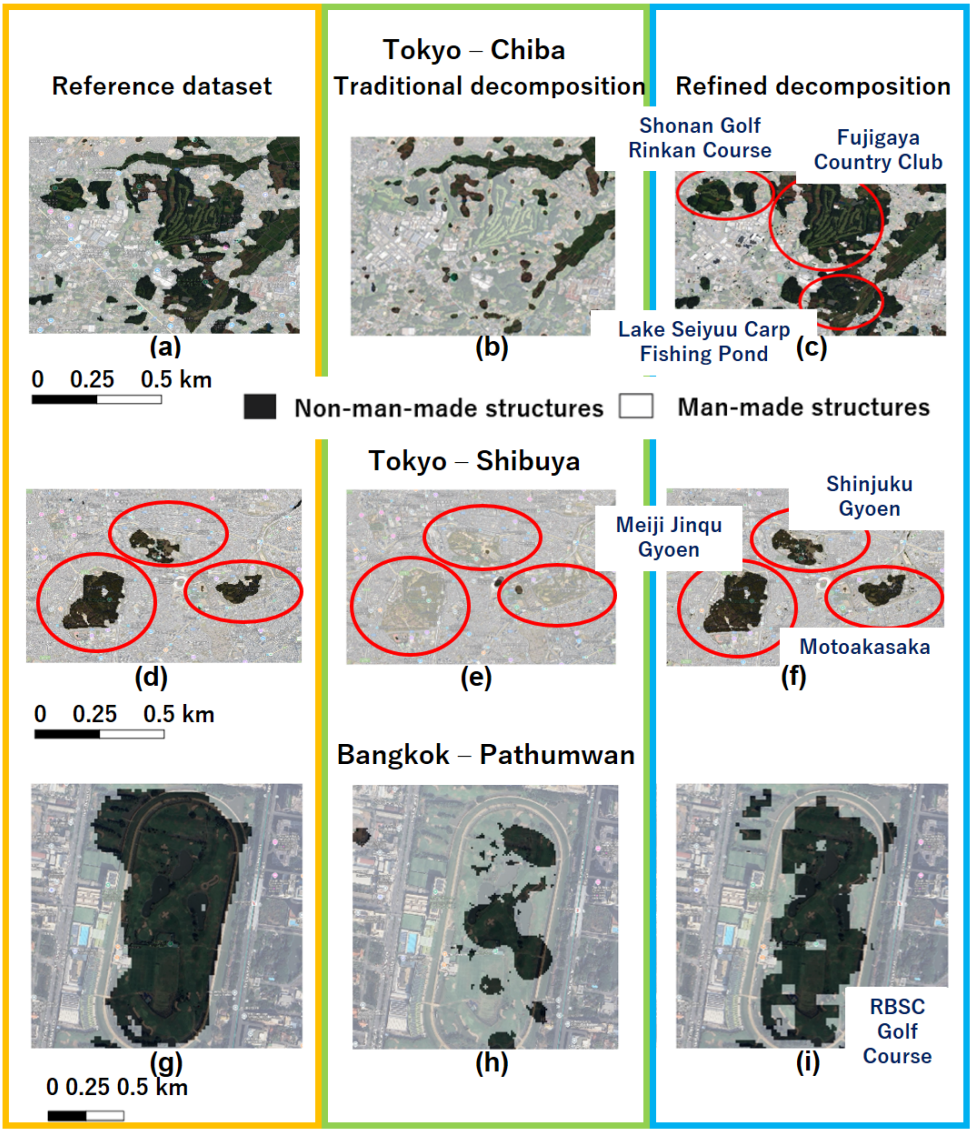

Figure 13. Comprehensive comparison of classification methods across three test sites. Left column (a, d, g): Sentinel-2 reference data; Middle column (b, e, h): Traditional Yamaguchi decomposition; Right column (c, f, i): Refined decomposition with POA correction. Top row: Tokyo-Chiba area with golf courses and fishing pond; Middle row: Tokyo-Shibuya area with urban parks; Bottom row: Bangkok-Pathumwan area with golf driving range. Red circles indicate areas where refinement successfully corrected misclassifications. Black: non-man-made structures; White: man-made structures.

5.3 City Comparison via Scattering Distributions

To assess the spatial transferability and robustness of the proposed classification approach, KL divergence was employed to quantify the statistical differences in Pd and Pv scattering distributions across land cover types in the three study areas: Tokyo, Bangkok, and Manila. This analysis reveals the different response of man-made structures and natural features to polarimetric decomposition depending on geographic and environmental contexts.

In the Tokyo–Bangkok comparison, high KL divergence was observed for water and agriculture classes, suggesting significant differences in their scattering behaviours. The water surfaces in Tokyo exhibited broader distribution curves, while Bangkok showed sharper, more peaked responses, likely reflecting more homogeneous surface conditions. Agricultural differences arose from variations in distribution peak positions, possibly because of differing crop types or land management practices influencing volume scattering. In contrast, man-made and forest classes showed lower divergence, indicating more consistent scattering properties between the cities.

Comparing Tokyo and Manila, the man-made class exhibited the highest divergence. The Pd and Pv distributionsin Tokyo showed pronounced peaks, likely because of uniform, high-rise concrete and steel structures with consistent alignment. In contrast, the distributions in Manila were more diffuse, likely reflecting its heterogeneous urban form comprising low-rise buildings, informal settlements, and diverse construction materials. Moderate divergence was also found in water and bare land categories, possibly driven by differences in hydrological and surface roughness characteristics. Simultaneously, forest and agriculture classes displayed relatively low divergence.

The Bangkok–Manila comparison showed the highest divergence in bare land and water classes. The bare land responses in Bangkok were sharply peaked, while those in Manila were more spread out, again pointing to differences in surface texture and environmental conditions. Lower divergence in agriculture and forest classes suggests similar vegetation structure or scattering mechanisms between these two cities.

Overall, the KL divergence results highlight the importance of city-specific considerations when applying classification models, particularly for natural land cover types. Man-made areas exhibited more stable scattering patterns between Tokyo and Bangkok but varied considerably between Tokyo and Manila. This suggests that while urban features often produce consistent scattering responses, differences in architectural style, building materials, and density can lead to significant statistical variation. Bangkok emerges as a transitional case, sharing structural characteristics with both Tokyo and Manila, which may explain the relatively lower divergence revealed through their comparison.

Acknowledging that variations in satellite sensor incidence angles influence observed scattering distributions is also essential. Even for structurally similar land cover types, differing look angles can alter the shape of Pd and Pv distributions, potentially affecting classification reliability if not properly corrected.

As shown in Figure 14, KL divergence values are the highest for water and agriculture between Tokyo and Bangkok, suggesting strong geometric or seasonal variability. Conversely, man-made areas show the greatest divergence between Tokyo and Manila, reflecting substantial differences in urban form and materials.

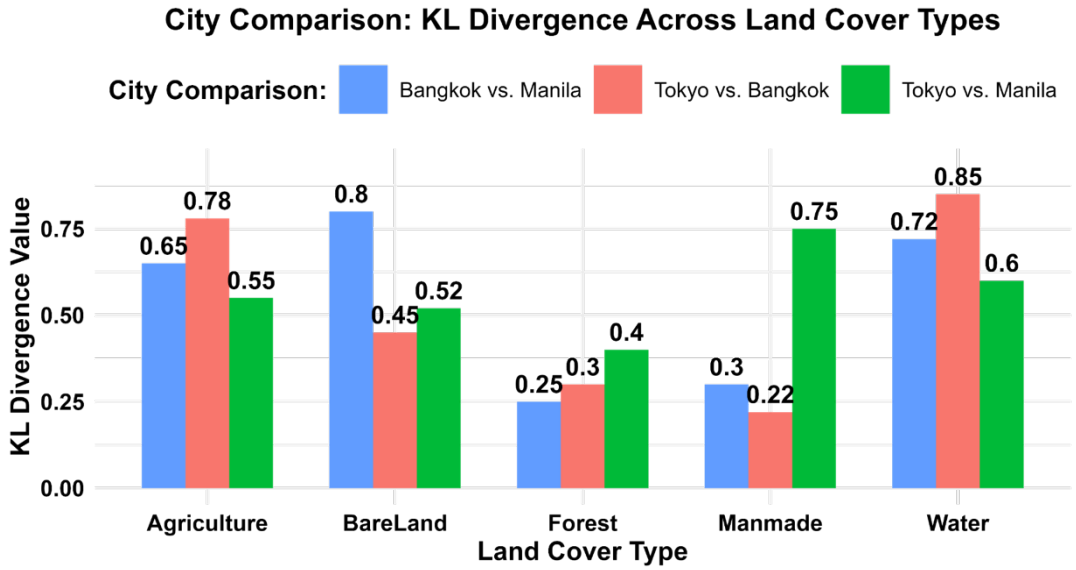

Figure 14. Kullback-Leibler (KL) divergence values across land cover types for each city pair (Tokyo–Bangkok, Tokyo–Manila, Bangkok–Manila). Water and agriculture show the largest divergence between Tokyo and Bangkok, while man-made areas exhibit the most distinct difference between Tokyo and Manila.

6. CONCLUSIONS

This study presented a novel physics-guided framework for extracting vertical man-made structures from PolSAR imagery. The core contribution of this work is not the application of standard machine learning algorithms, but the development of a methodological pipeline that integrates controlled experimental understanding with spaceborne SAR processing to address the fundamental problem of orientation-induced scattering ambiguities in urban areas.

A central contribution is the incorporation of Polarimetric Orientation Angle (POA) correction and refinement of the four-component decomposition. Compared with directly using the original polarimetric scattering (HH, HV, VV), the decomposition provides a more physically interpretable framework that better represents double-bounce, surface, and volume scattering behaviours. The adjustments applied to these components are grounded in backscattering physics, ensuring that vertical urban structures are more clearly separated from natural features, while still preserving sensitivity to vegetation and bare surfaces.

The proposed refinement achieved consistently high accuracies in diverse urban contexts 94.4% in Tokyo, 95.5% in Bangkok, and 95.6% in Manila with notable improvements in areas where urban and vegetated features are intermixed. These results indicate that the method

effectively captures the physical scattering mechanisms of urban targets across scenes with varying morphology and environmental complexity.

Importantly, this framework is not bound to any specific classifier. While k-means and random forest were employed in this study, the decomposition-based refinements can readily be paired with more advanced classification methods as they become available. This flexibility underlines the robustness of the proposed approach as a physically interpretable and adaptable strategy for urban feature extraction.

Despite these advances, the performance of the method remains influenced by scene-dependent parameters such as incidence angle, surface roughness, and urban morphology. The method is most reliably applied to high-density urban areas; its performance in low-density or peri-urban environments warrants further investigation. Future work should focus on fully automating the refinement process and further investigating the role of Ps in urban contexts to improve discrimination of roads and flat surfaces.

ACKNOWLEDGMENTS

This research was supported by a Grant-in-Aid for Scientific Research (KAKENHI) (C) (24K07712), The Kajima Foundation, Japan, Technical Research and Development for Road Policy Quality Improvement, Ministry of Land, Infrastructure, Transport, and Tourism (MLIT), Japan and the 4th Research Announcement on the Earth Observations of the Japan Aerospace Exploration Agency (JAXA).

REFERENCES

Attri, L., S. K. Singh, and S. Maithani. 2024. "Machine learning based urban land cover classification using PolInSAR data: A study with ALOS-2 and RADARSAT-2 datasets." *Discover Geoscience* 2, no. 29

Breiman, L. 2001. "Random forests." *Machine Learning* 45, no. 1: 5–32

Cloude, S. R., and E. Pottier. 1996. "A review of target decomposition theorems in radar polarimetry." *IEEE Transactions on Geoscience and Remote Sensing* 34, no. 2: 498–518.

Fang, Y., H. Zhang, Q. Mao, and Z. Li. 2018. "Land cover classification with GF-3 polarimetric synthetic aperture radar data by random forest classifier and fast super-pixel segmentation." *Sensors* 18, no. 7: 2014.

Freeman, A., and S. L. Durden. 1998. "A three-component scattering model for polarimetric SAR data." *IEEE Transactions on Geoscience and Remote Sensing* 36, no. 3: 963–973.

Hariharan, S., S. Tirodkar, and A. Bhattacharya. 2016. "Polarimetric SAR decomposition parameter subset selection and their optimal dynamic range evaluation for urban area classification using Random Forest." *International Journal of Applied Earth Observation and Geoinformation* 44: 144–158.

Japan Aerospace Exploration Agency (JAXA). 2021a. "ALOS-2/PALSAR-2: Overview." Earth Observation Research Center (EORC).

https://www.eorc.jaxa.jp/ALOS-2/en/about/palsar2.htm

Japan Aerospace Exploration Agency (JAXA). 2021b. "PALSAR-2 Level 1.1/2.1/1.5/3.1 CEOS SAR Product Format Description." Revision E. https://www.eorc.jaxa.jp/ALOS/en/alos-2/pdf/product_format_description/PALSAR-2_xx_Format_CEOS_E_g.pdf

Kajimoto, M., and J. Susaki. 2013. "Urban density estimation from polarimetric SAR images based on a POA correction method." *IEEE Journal of Selected Topics in Applied Earth Observations and Remote Sensing* 6, no. 3: 1418–1429.

Karra, K., C. Kontgis, Z. Statman-Weil, J. C. Mazzariello, M. Mathis, and S. P. Brumby. 2021. "Global land use/land cover with Sentinel-2 and deep learning." In Proceedings of the 2021 *IEEE International Geoscience and Remote Sensing Symposium (IGARSS)*, 4704–4707.

Kimura, H. 2008. "Radar polarization orientation shifts in built-up areas." *IEEE Geoscience and Remote Sensing Letters* 5, no. 2: 217–221.

Lee, J.-S., and E. Pottier. 2009. *Polarimetric Radar Imaging: From Basics to Applications*. CRC Press.

Lee, J.-S., D. L. Schuler, and T. L. Ainsworth. 2002. "On the estimation of radar polarization orientation shifts induced by terrain slopes." *IEEE Transactions on Geoscience and Remote Sensing* 40, no. 1: 30–41.

Li, H., Q. Li, G. Wu, J. Chen, and S. Liang. 2016. "The impacts of building orientation on polarimetric orientation angle estimation and model-based decomposition for multilook polarimetric SAR data in urban areas." *IEEE Transactions on Geoscience and Remote Sensing* 54, no. 9: 5520–5532.

Schmitt, M., and X. X. Zhu. 2016. "Data fusion and remote sensing: An ever-growing relationship." *IEEE Geoscience and Remote Sensing Magazine* 4, no. 4: 6–23.

Singh, G., Y. Yamaguchi, and S.-E. Park. 2013. "General four-component scattering power decomposition with unitary transformation of coherency matrix." *IEEE Transactions on Geoscience and Remote Sensing* 51, no. 5: 3014–3022.

United Nations, Department of Economic and Social Affairs, Population Division. 2019. *World Urbanization Prospects: The 2018 Revision.* United Nations.

Weng, Q. 2012. "Remote sensing of impervious surfaces in the urban areas: Requirements, methods, and trends." *Remote Sensing of Environment* 117: 34–49.

Yamaguchi, Y. 2020. *Polarimetric SAR Imaging: Theory and Applications*. CRC Press.

Yamaguchi, Y., G. Singh, and H. Yamada. 2018. "On the model-based scattering power decomposition of fully polarimetric SAR data." *IEICE Transactions on Communications* J101-B, no. 9: 638–647.

Yamaguchi, Y., Y. Yajima, and H. Yamada. 2006. "A four-component decomposition of POLSAR images based on the coherency matrix." *IEEE Geoscience and Remote Sensing Letters* 3, no. 3: 292–296.

Zou, T., W. Yang, D. Dai, and H. Sun. 2010. "Polarimetric SAR image classification using multifeatured combination and extremely randomized clustering forests." *EURASIP Journal on Advances in Signal Processing* 2010: 465612.